Iron cycle interactions with hydrological dynamics reduce methane production in a simulated Arctic soil

Benjamin N. Sulman[1], Fengming Yuan[1], Teri O'Meara[1], Baohua Gu[1], Elizabeth Herndon[1], Jianqiu Zheng[3], Peter Thornton[1], and David E. Graham[2]

1. Climate Change Science Institute and Environmental Sciences Division, Oak Ridge National Laboratory
2. Biosciences Division, Oak Ridge National Laboratory
3. Biological Sciences Division, Pacific Northwest National Laboratory

Key Points:

- Ferric iron reduction can fuel decomposition in iron-rich Arctic soils. Higher rates of iron reduction can reduce methane production
- We coupled iron and carbon cycling in a geochemical reaction model and simulated repeated flooding and draining of Arctic soils
- More frequent cycling of flooding and drainage reduced methane emissions and increased carbon dioxide production by recycling iron

Abstract:

The fate of organic carbon (C) in permafrost soils is important to the climate system due to the large global stocks of permafrost C. Thawing permafrost can be subject to dynamic hydrology, making anaerobic processes an important factor controlling soil organic matter (SOM)

decomposition rates and greenhouse gas production. In iron (Fe)-rich permafrost soils, Fe(III) can serve as a terminal electron acceptor, suppressing methane (CH_4) production and increasing carbon dioxide (CO_2) production. Current large-scale models of Arctic C cycling do not include Fe cycling or pH interactions. Here, we coupled Fe redox reactions and C cycling in a geochemical reaction model to simulate the interactions of SOM decomposition, Fe(III) reduction, pH dynamics, and greenhouse gas production in permafrost soils subject to dynamic hydrology. We evaluated the model using measured CO_2 and CH_4 fluxes as well as changes in pH, Fe(II), and dissolved organic matter concentrations from oxic and anoxic incubations of permafrost soils from polygonal permafrost sites in northern Alaska, United States. In simulations of oxic-anoxic cycles, rapid oxidation of Fe(II) to Fe(III) during oxic periods and gradual Fe(III) reduction during anoxic periods reduced cumulative CH_4 fluxes and increased cumulative CO_2 fluxes in simulations with higher frequency oxic-anoxic cycling. Lower pH suppressed CH_4 fluxes through its direct impact on methanogenesis and by increasing Fe(III) bioavailability. Our results suggest that models that do not include Fe(III) reduction and its pH dependence could overestimate CH_4 production and underestimate CO_2 emissions and SOM decomposition rates in Fe-rich, frequently flooded Arctic soils.

Plain language summary

Soils in cold regions store large amounts of carbon that may be converted to climate-warming greenhouse gases as frozen soils thaw. Methane, a powerful greenhouse gas, is primarily produced when soils are flooded and lack oxygen. However, Arctic soils are also rich in iron, which some soil organisms can use instead of oxygen through a decomposition pathway that also produces carbon dioxide rather than methane. The computer models that are currently used to predict greenhouse gas emissions from thawing Arctic soils do not include iron interactions. We built a new model to simulate how iron, oxygen, and carbon interact in soils that are repeatedly flooded and drained. We tested the model using laboratory measurements of greenhouse gas production and iron cycling in Arctic soils. Our model simulations showed that when soils cycle more often between being flooded and exposed to air, iron is recycled to forms that can fuel carbon dioxide production while reducing methane gas production. Our results suggest that including iron cycling in soil carbon models could improve predictions of the climate warming potential of greenhouse gas emissions from thawing Arctic soils.

1. Introduction

Permafrost regions contain enormous soil organic carbon (C) stocks (Hugelius et al., 2014). The fate of this vast C pool is critical to the global climate system because of the potential for decomposition of permafrost organic matter (OM) and C release into the atmosphere as greenhouse gases (Schuur et al., 2015; Turetsky et al., 2020). Because thawing permafrost often drives physical collapse and flooding, anoxic processes are an important component of permafrost OM decomposition. Major uncertainties in current understanding of permafrost thaw include the amount of C that will be mineralized and the relative amounts of CO_2 and CH_4 that will be produced by decomposition of OM in thawing permafrost soils.

Decomposition processes in saturated Arctic soils are tightly coupled to cycling of other elements including oxygen (O), nitrogen (N), and iron (Fe), which can serve as terminal electron acceptors (Dettling et al., 2006; Lipson et al., 2010). The presence of electron acceptors such as Fe(III) has been shown to suppress the production of CH_4, which provides a lower energy benefit to microbial metabolism, when Fe reducers are able to outcompete methanogens for substrates (Lipson et al., 2012; Miller et al., 2015). Simultaneous methanogenesis and ferric Fe (Fe(III)) reduction have been observed in Arctic soils, however, indicating that microbial processes do not necessarily strictly follow the redox ladder (Roy Chowdhury et al., 2015; Herndon et al., 2015; Yang et al., 2016; Reiche et al., 2008; Zheng et al., 2018). Many Arctic soils are rich in Fe(III)-bearing minerals and OM-bound Fe(III), and as a result, redox cycling of Fe can be an important control on OM degradation and C mineralization in permafrost soils (Herndon et al., 2017). Terminal electron acceptor availability and CH_4 production are also strongly dependent on soil pH (Zheng et al., 2019).

Despite the importance of such redox cycling processes for determining organic matter decomposition and greenhouse gas production in Arctic soils, the models applied at ecosystem to global scales to predict C cycling and related climate change feedbacks do not explicitly represent redox processes or pH dynamics (Wang et al., 2019; Wania et al., 2013; Xu et al., 2016). This omission opens the possibility that model projections could overestimate CH_4 emission and underestimate organic C mineralization and CO_2 production rates in soils where alternate terminal electron acceptors are abundant. Such bias could be amplified in soils with dynamic hydrology that drives oscillations in redox conditions and consequent fluctuations in terminal electron acceptor variability.

Here, we simulated coupled OM decomposition and Fe redox cycling in the reactive transport model PFLOTRAN (Hammond et al., 2014). PFLOTRAN has been applied in biogeochemical contexts such as hyporheic zones (Dwivedi et al., 2018), and has previously been directly coupled to a land surface model and used to simulate soil organic matter cycling (Tang, Yuan, et al., 2016). We parameterized a biogeochemical reaction network using laboratory incubations of permafrost soils collected from different layers and microtopographic settings in a polygonal permafrost landscape, and then used the model to investigate how interactions between C and Fe cycling affect CH_4 and CO_2 production over oxic-anoxic cycles across a range of soil pH.

2. Methods

2.1. Model simulations

Simulations were conducted using a reaction network defined in PFLOTRAN (Figure 1, Table 1) building on reaction network developments from previous modeling studies using a different chemical reaction model, PHREEQC (Tang, Zheng, et al., 2016; Zheng et al., 2019) and previous implementation of soil organic matter decomposition reactions in PFLOTRAN (Tang, Yuan, et al., 2016). Organic matter pools in the reaction network included solid soil organic matter (SOM) and dissolved organic matter (DOM). Solid organic matter was first hydrolyzed to DOM, which could then be completely oxidized to CO_2 through aerobic decomposition (consuming O_2) or decomposed to produce organic acids (represented in the model by acetate) and CO_2 through fermentation (in anoxic conditions). Acetate could be mineralized either by microbial reduction of Fe(III) or by acetoclastic methanogenesis. Aqueous Fe(III) ions were equilibrated with amorphous $Fe(OH)_3$ minerals through kinetic precipitation and dissolution reactions, which were calculated using Transition State Theory type rate laws (Dwivedi et al., 2018). These precipitation-dissolution relationships were highly pH dependent, with extremely low concentrations of uncomplexed aqueous Fe(III) ions under typical pH conditions. The model included equilibrium aqueous complexes of Fe(III) with DOM and acetate, which greatly increased the concentration of total aqueous Fe(III). However, note that in PLFOTRAN, aqueous chemical reaction rates, including Fe(III) reduction rates, are calculated based on free ion concentrations rather than total aqueous concentrations. Fe(III) reduction converted Fe(III) to

more soluble ferrous Fe (Fe(II)) ions. Under oxic conditions, Fe(II) was rapidly oxidized back to Fe(III). Fe(III) reduction and Fe(II) oxidation effectively functioned as reductive dissolution and oxidative precipitation of $Fe(OH)_3$ due to the tight coupling between the aqueous and mineral phases.

Methanogenesis was simulated as a combination of acetoclastic and hydrogenotrophic pathways. pH dependence of the two methane pathways were determined based on an optimization to measurements of Kotsyurbenko et al. (2007) (Figure S1). The optimized pH dependence had the form:

$$F(pH) = \frac{10^{-pH}}{10^{-pH}+10^{-k_1}} \frac{10^{-k_2}}{10^{-pH}+10^{-k_2}} \quad (1)$$

Where $F(pH)$ is relative flux as a function of pH for either methanogenesis pathway, and k_1 and k_2 are parameters determining limitation by low and high pH, respectively. For acetoclastic methanogenesis, the optimization found k_1 and k_2 both equal to 5.5. For hydrogenotrophic methanogenesis, the optimization found $k_1 = 6.75$ and $k_2 < 0$, indicating no limitation at low pH. Methanogenesis was inhibited by the presence of Fe(III) and O_2, which represented more energetically favorable terminal electron acceptors. This approach assumes that simultaneous Fe(III) reduction and methanogenesis is limited, which is consistent with the traditional redox ladder conceptual model but may not be accurate for systems where simultaneous methanogenesis and Fe(III) reduction are common as noted above. SOM aerobic decomposition and anaerobic hydrolysis followed CLM-CN decomposition kinetics (Tang, Yuan, et al., 2016) modified to allow Monod and inverse Monod (inhibition) responses to aqueous chemical species and assuming no nitrogen limitation of decomposition. Microbial aqueous reactions were assumed to follow multi-Monod kinetics of the form:

$$R = V_{max} \prod_N \frac{C_{S_N}}{K_{S_N}+C_{S_N}} \prod_M \frac{K_{I_M}}{K_{I_M}+C_{I_M}} \quad (2)$$

where R is reaction rate (mol (L H_2O)$^{-1}$ s^{-1}), V_{max} is maximum reaction rate (mol L^{-1} s^{-1}), N is the set of reactant species (including substrates and terminal electron acceptors), M is the set of inhibiting species, C_{S_N} is the concentration of the Nth substrate, K_{S_N} is the half-saturation constant of the Nth substrate, C_{I_M} is the concentration of the Mth inhibiting species, and K_{I_M} is the inhibition constant of the Mth inhibiting species.

In addition to the kinetic reactions described above, the reaction network included the pH buffering effect of soil organic matter. The soil matrix was assumed to contain surface complexation sites that could exchange H^+ ions under changing pH conditions. The volumetric density of these proton exchange sites was proportional to organic matter concentration in the soil layer being simulated (following Zheng et al., 2019) and the fraction of sorbed H^+ followed equilibrium sorption kinetics as defined in PFLOTRAN (https://www.pflotran.org/documentation/theory_guide/mode_reactive_transport.html).

Aerated and saturated conditions were simulated by varying the diffusion rate of O_2 between the simulated soil layer and a boundary condition representing aqueous O_2 concentration at equilibrium with the atmosphere. Flux was calculated based on the difference between O_2 concentration in the soil layer and in the boundary condition:

$$F_{O_2} = \left(\frac{[O_2]_{sat} - [O_2]_S}{\Delta z}\right) k_d \quad (3)$$

where F_{O_2} is flux rate of O_2 between the soil porewater and boundary condition (mol cm^{-2} s^{-1}), $[O_2]_{sat}$ is the aqueous O_2 concentration at saturation with respect to the atmosphere (mol cm^{-3}), $[O_2]_S$ is the soil aqueous O_2 content, Δz is the soil layer thickness (cm), and k_d is the diffusion coefficient (cm^2 s^{-1}). Under aerated conditions, k_d was set to 0.1 cm^2 s^{-1}, and under saturated conditions, k_d was set to zero, preventing O_2 from being replenished. For purposes of gas diffusion, Δz was assumed to be 10 cm. For simplicity, soil water content was assumed to be constant and equal to porosity across aerated and saturated conditions. This assumption prevented the model from simulating changes in aqueous concentrations driven only by differences in water content associated with drying.

Table 1: Porewater reactions included in the model. Monod and inhibition species are followed by the half-saturation concentration (M, mol L^{-1}) in parentheses. DOM is expressed per mol C and is assumed to have a stoichiometry 6 C:12 H:6 O.

Reaction	Stoichiometry	Reaction type	Reaction rate parameter (s^{-1} for	Monod species (half-saturation	Inhibition species (inhibition

			SOM and M s^{-1} for Monod)	concentration [M])	constant [M])
SOM hydrolysis	SOM-C + H_2O → DOM-C	SOM	$1.0x10^{-8}$		DOM (0.5)
Fermentation	DOM-C +0.33 H_2O → 0.33 CH_3COO^- + 0.33 CO_2^- + 0.33 H^+ + 0.67 H_2	Monod	$4.0x10^{-7}$	DOM-C (0.5)	Acetate (0.04) O_2 (10^{-5})
DOM aerobic respiration	DOM-C + O_2 → CO_2 + H_2O	Monod	$5.0x10^{-7}$	O_2 (10^{-4}) DOM-C (0.5)	
Acetate aerobic respiration	CH_3COO^- + 2 O_2 + H^+ → 2 CO_2 + 2 H_2O	Monod	$5.0x10^{-7}$	O_2 (10^{-4}) Acetate (0.04)	
Fe(III) reduction	CH_3COO^- + 8 Fe^{3+} + 2 H_2O → 2 CO_2 + 8 Fe^{2+} + 7 H^+	Monod	$3.0x10^{-8}$	Acetate (0.04) Fe(III) (10^{-10})	O_2 (10^{-5})
Fe(II) oxidation	Fe^{2+} + 0.25 O_2 + H^+ → Fe^{3+} + 0.5 H_2O	Monod	$1.0x10^{-6}$	O_2 (10^{-4}) Fe(II) (0.1)	
Acetoclastic methanogenesis	CH_3COO^- + H^+ → CH_4 + CO_2	Monod	$2.0x10^{-8}$	Acetate (0.04) H^+ ($10^{-5.5}$)	O_2 (10^{-5}) Fe(III) (10^{-10}) H^+ ($10^{-5.5}$)
Hydrogenotrophic methanogenesis	4 H_2 + CO_2 → CH_4 + 2 H_2O	Monod	$9.6x10^{-9}$	H_2 (0.1) HCO_3^- (0.1)	O_2 (10^{-5}) Fe(III) (10^{-10})

					H^+ ($10^{-6.75}$)
H_2 oxidation	$2\ H_2 + O_2 \rightarrow 2\ H_2O$	Monod	$1.0x10^{-6}$	H_2 (0.1) O_2 (10^{-4})	
$Fe(OH)_3$	$Fe(OH)_3 + 3\ H^+ \leftrightarrow Fe^{3+} + 3\ H_2O$	Precipitation-dissolution	$1.0x10^{-6}$ mol m^{-2} surface area s^{-1}		
*$Fe(OH)_3$ reductive dissolution	$Fe(OH)_3 + 0.125\ CH_3COO^- + 2.125\ H^+ \rightarrow 2.75\ H_2O + 0.25\ CO_2 + Fe^{2+}$				
*$Fe(OH)_3$ oxidative precipitation	$Fe^{2+} + 0.25\ O_2 + 2.5\ H_2O \rightarrow Fe(OH)_3 + 2\ H^+$				

*The $Fe(OH)_3$ reductive dissolution and oxidative precipitation equations are represented in the model through separate precipitation-dissolution and oxidation/reduction steps but the combined stoichiometries are shown here to ease interpretation of their effects on pH.

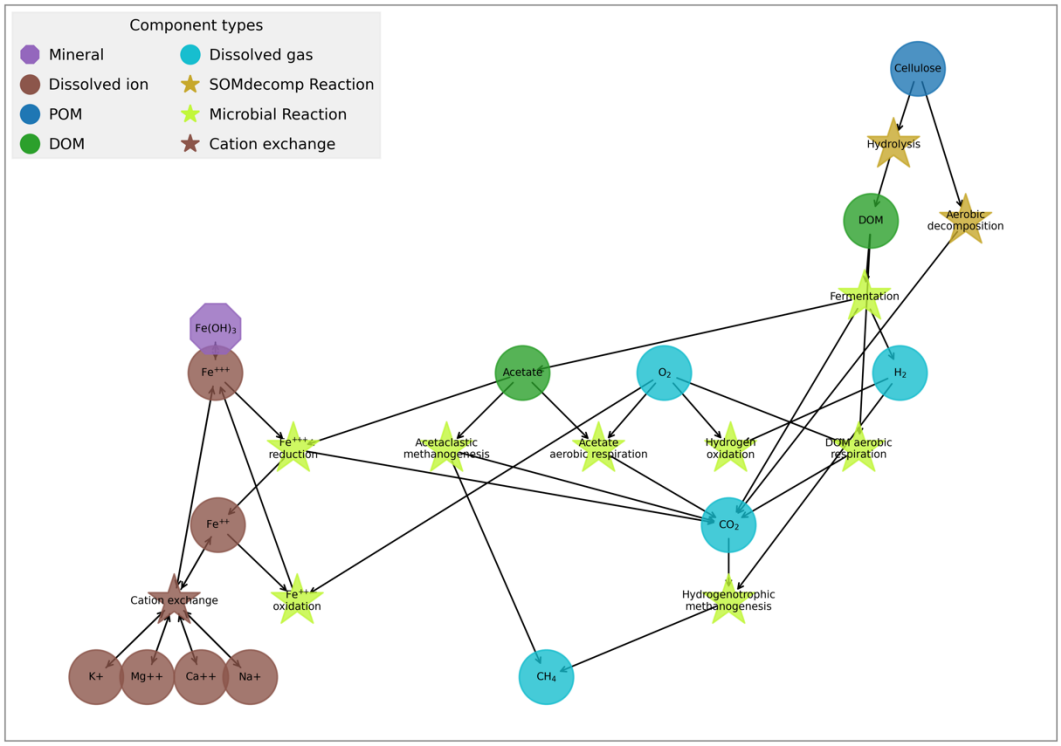

Figure 1: Network diagram of reactions included in the PFLOTRAN reaction network. Circles show chemical pools, and stars show reactions. Some chemical species, including H^+, are omitted for clarity.

2.2. Comparison with incubation measurements

Model simulations were parameterized using measurements from laboratory incubations of seasonally thawed soil from the active layer of permafrost-underlain polygons, as synthesized by Zheng et al. (2018, 2019) and porewater chemistry measurements from Herndon et al. (2016). Soil cores were collected from Utqiagvik, Alaska and include trough, ridge, and center locations in ice-wedge polygons. Incubations included an oxic incubation of a high-centered polygon center organic horizon and anoxic incubations of organic and mineral horizons from a trough and a rim location. Reported data include head space CH_4 and CO_2 concentrations over time, pH, DOM, organic acid, and aqueous Fe(II) concentrations.

Model rate constants and key parameters were adjusted to maximize agreement (based on root mean square error (RMSE) and correlation coefficient (R)) between modeled and measured time series of CO_2 flux, CH_4 flux, pH, and concentrations of Fe(II), DOM, and organic acids

(compared with acetate in the model) across four incubations with the multiple time points of the relevant measurements. Fermentation rate constant and half-saturation (K_S) for acetate were identified as particularly sensitive parameters, and simulations were conducted across a range of these parameters to identify the optimal values (Figs. S2 and S3). The same rate constants and half-saturation constants were applied to all horizons. Simulated incubations were initialized using available measurements from each incubation. SOC and bulk density were determined using measured SOC, assuming bulk density followed the relation of (Bockheim et al., 2003):

$$BD = e^{\frac{8.2432 - SOC(\%)}{9.7872}} \quad (4)$$

where SOC (%) is SOC in mass percentage and BD is bulk density in units of g cm^{-3}. Note that since measurements were expressed per unit dry soil mass, the lack of reported bulk density measurements means that any mismatch between actual and measured bulk density would introduce error to model-measurement comparisons.

Soil pH at the beginning of the simulated incubation was set as the measured pH at time zero of the incubation. Initial aqueous Fe(II) concentration was set as the measured aqueous Fe(II) concentration at time zero, and initial Fe oxide mineral mass was set to 1.5 times the increase in measured Fe(II) concentration (per unit soil mass) over the course of the incubation, thereby assuming that two thirds of initial Fe oxides were reduced to Fe(II) over the course of each incubation. This correction was based on the assumption that some fraction of the Fe oxides were not reduced over the course of the incubations, likely representing crystalline oxides that are more resistant to microbial reduction, and aligned $Fe(OH)_3$ concentrations in the model with measurements of total extractable Fe from similar soils (Herndon et al., 2017). Initial DOM and acetate concentrations were set using measured DOM and organic acid concentrations, respectively. Cation exchange capacity (CEC) was set using SOC content, assuming that CEC of organic matter was 200 meq $(100\ g)^{-1}$ and CEC of mineral material was 25 meq $(100\ g)^{-1}$ (Ping et al., 1998). Initial hydrolysable SOC was set using measured SOC, assuming that hydrolysable SOC represented 5% of total SOC (consistent with a small labile fraction; Schädel et al., 2013). Initial concentrations of Mg^{2+}, Ca^{2+}, Na^{+}, and K^{+} were set using mean porewater chemistry measurements from (Herndon et al., 2015, 2016).

2.3. Simulated oxic-anoxic cycling

Oxic-anoxic cycles were simulated by varying the k_d over time to represent transitions between aerated and saturated states. k_d was changed instantaneously at the time of transition between aerated and saturated conditions. Simulations were conducted over a 150-day period, with 10% of the simulation time spent under aerated conditions. Simulations with only one cycle started under aerated conditions and then remained under saturated conditions for the remainder of the simulation. Simulations with multiple cycles shortened the length of each aerated period so that the total time under aerated and saturated conditions was the same (15 days under aerated conditions) in all simulations. The effect of pH was tested by repeating simulations with initial pH conditions ranging in increments of 0.5 from 4.5 to 6.0, a range typical of Arctic tundra soils. These simulations were conducted for one organic horizon and one mineral horizon from the trough of a permafrost-underlain low-centered polygon initialized using data from incubation cores as described below.

3. Results

3.1. Comparison of model simulations and incubations

Model simulations generally compared well with observations (Figure 2). Simulated CO_2 production was on the same order as measured fluxes except for the rim organic horizon where all rates were overestimated. This overestimation may have been due to the high organic content (39%) and consequently low calculated bulk density (0.28 g cm^{-3}) of that profile, which meant that fluxes expressed on a per-weight basis were divided by a small mass. Note that the model simulated cumulative production of CO_2 and CH_4 in porewater and did not explicitly simulate transport of dissolved gases across the soil surface to the head space. CH_4 production matched well between model and measurements, although the model overestimated the rate of increase and maximum rate in the organic horizon from the rim core (Fig. 2h). The model did reproduce the gradual increase in CH_4 flux rate observed in the trough organic and mineral horizons (Fig. 2g,i). Model simulations matched well with the rate of increase in Fe(II) concentrations for all anoxic incubations except the rim organic horizon, which was overestimated. While measurements of Fe oxide and sorbed Fe concentrations were not available, the model simulations produced reasonable changes over time, with Fe oxide minerals gradually depleting

in favor of dissolved and sorbed Fe(II) over the course of anoxic incubations. In the oxic incubation of the center organic horizon, the model simulated a very rapid decline in Fe(II) concentrations as Fe(II) was rapidly oxidized to Fe(III) (Fig. 2k). The model did not reproduce the higher Fe(II) concentration observed later in the oxic incubation. The model reproduced measured increases in pH during the Fe(III) reduction phase in the trough cores but not in the rim cores. Simulated concentrations of DOM and acetate were generally accurate, although the model did not reproduce the observed decline in acetate concentrations over time in the mineral horizons and trough organic horizon.

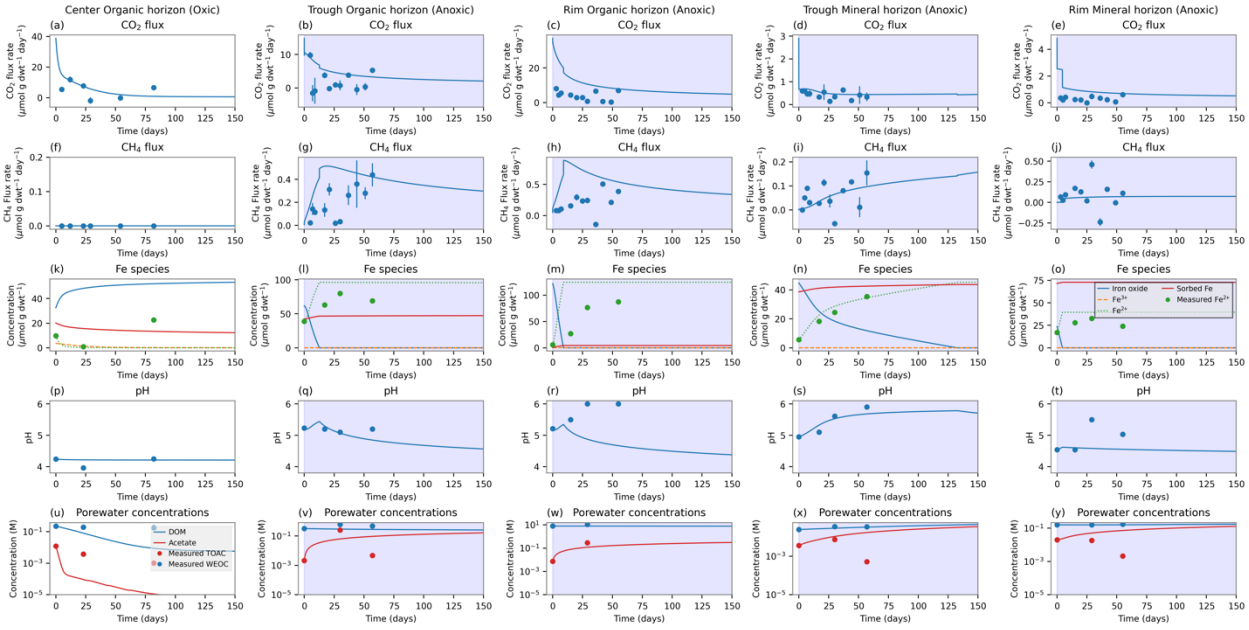

Figure 2: Comparison between incubation measurements and model simulations. Each column shows results from an individual incubation. Each row shows a different measured quantity. Lines show model simulation results and circles show measurements (Zheng et al., 2018, 2019). Oxic conditions are shown with a white background and anoxic conditions are shown with a blue background.

3.2. Simulations of wetting-drying cycles

Simulations of repeated oxic-anoxic cycles highlighted the succession of decomposition phases as the system depleted different terminal electron acceptors, as well as the interaction of these phases with pH (Fig. 3, S4). During oxic periods, CO_2 fluxes were high, supported by abundant

279 oxygen (Fig. 3b). During anoxic periods, O_2 was rapidly depleted, causing a sharp decline in
280 CO_2 production rate. Early in each anoxic period, Fe(III) reduction increased quickly, as shown
281 by the production rate of Fe(II) ions (Fig. 3c). Fe(III) reduction depleted Fe oxide minerals (Fig.
282 3d) and increased pH (Fig. 3e) due to the net proton consumption effect of $Fe(OH)_3$ reductive
283 dissolution (Table 1). CH_4 fluxes (Fig 3a) were inhibited by Fe(III), delaying the increase in CH_4
284 production rates under anoxic conditions. Fe(III) reduction produced twice as much CO_2 per unit
285 acetate consumed as methanogenesis and had a faster reaction rate, causing CO_2 production to be
286 higher during the Fe(III) reduction phase than during the methanogenesis phase. The temporal
287 pattern of Fe(III) reduction and its effect on methanogenesis were controlled by a combination of
288 Fe(III) accessibility and pH. Under lower pH conditions (dotted lines), Fe oxide mineral
289 solubility was higher, leading to higher Fe(III) availability and consequently more rapid Fe(III)
290 reduction rates and stronger inhibition of methanogenesis. Under higher pH conditions (solid and
291 dashed lines), the lowered Fe oxide solubility, combined with the rise in pH driven by Fe oxide
292 dissolution, inhibited further Fe(III) reduction. Rising pH allowed methanogenesis rates to
293 increase over time in simulated mineral horizons (Fig. 3) while methanogenesis rates increased
294 after depletion of soluble Fe oxides in simulated organic horizons (Fig. S4).
295

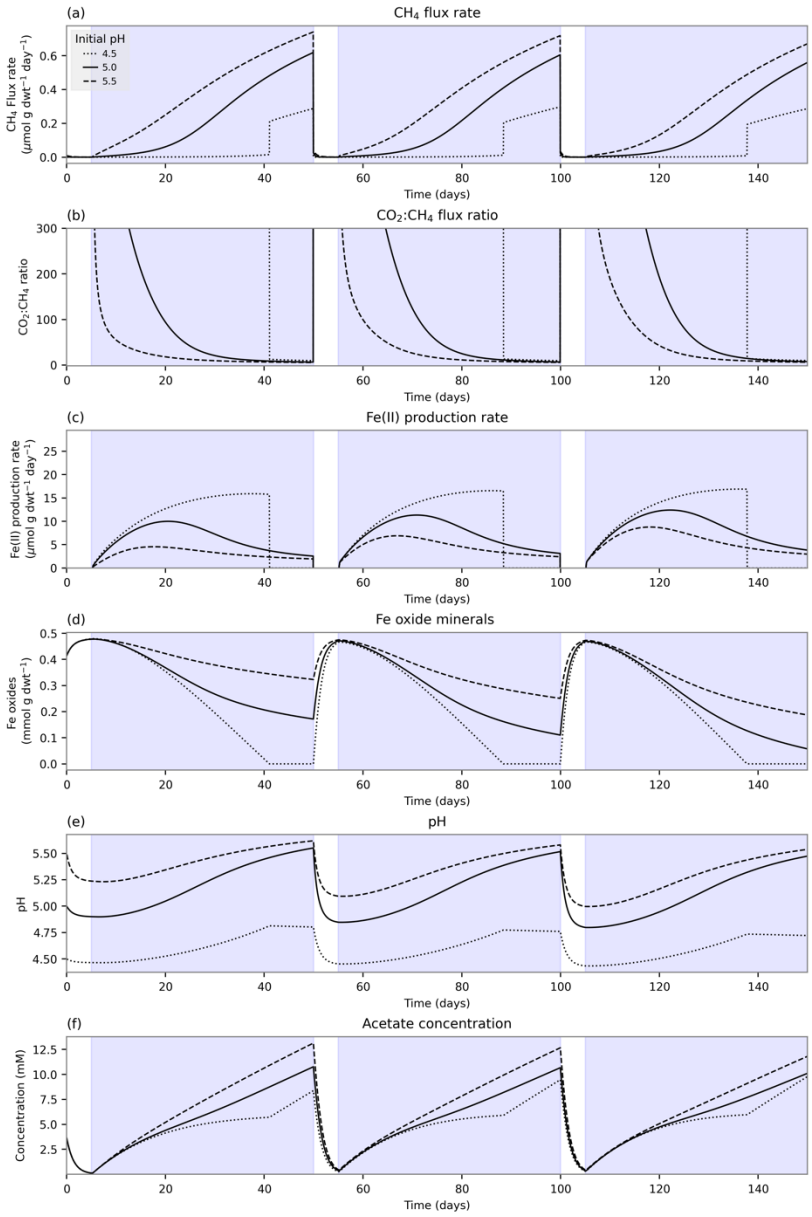

Figure 3: Simulated oxic-anoxic cycles for a mineral horizon. Blue backgrounds indicate saturated conditions and white backgrounds indicate aerated conditions. (a): CH_4 flux rate. (b): Ratio of CO_2 flux rate to CH_4 flux rate. Note that at pH 4.5 this ratio is outside the axis bounds (> 800) due to the low CH_4 flux rate. (c): Fe(II) production rate via Fe(III) reduction. (d): Fe oxide mineral concentration. (e): pH. (f): Acetate concentration.

Integrating CO_2 and CH_4 fluxes across multiple oxic-anoxic cycles showed the cumulative impact of the Fe-C-pH interactions on CO_2 and CH_4 fluxes (Fig. 4). Integrated CO_2 fluxes increased with more oxic-anoxic cycles, with a stronger increase in the simulated organic than in

306 the simulated mineral horizon (Fig. 4a). Cumulative CO_2 fluxes were minimally affected by pH.
307 The total increase in cumulative CO_2 production from one to four cycles was approximately 2.4
308 mmol g dwt^{-1} (a 120% increase relative to one cycle) in the organic horizon and 0.59 mmol g
309 dwt^{-1} (a 100% increase) in the mineral horizon.
310 Cumulative CH_4 production declined with increasing numbers of oxic-anoxic cycles. At
311 pH of 6, CH_4 fluxes declined from 0.16 to 0.09 mmol g dwt^{-1} (45%) between one and four
312 cycles, and at pH of 4.5 integrated CH_4 fluxes declined from 0.055 to 0.035 mmol g dwt^{-1} (35%).
313 In the mineral horizon, CH_4 flux declined from 0.09 to 0.03 mmol g dwt^{-1} (66%) at pH of 6.0 and
314 was eliminated entirely at pH of 4.5 and multiple oxic-anoxic cycles. Note that while the
315 fractional changes in CH_4 fluxes were comparable with the fractional changes in CO_2 fluxes, the
316 magnitude of C flux change was an order of magnitude higher for CO_2 than for CH_4.

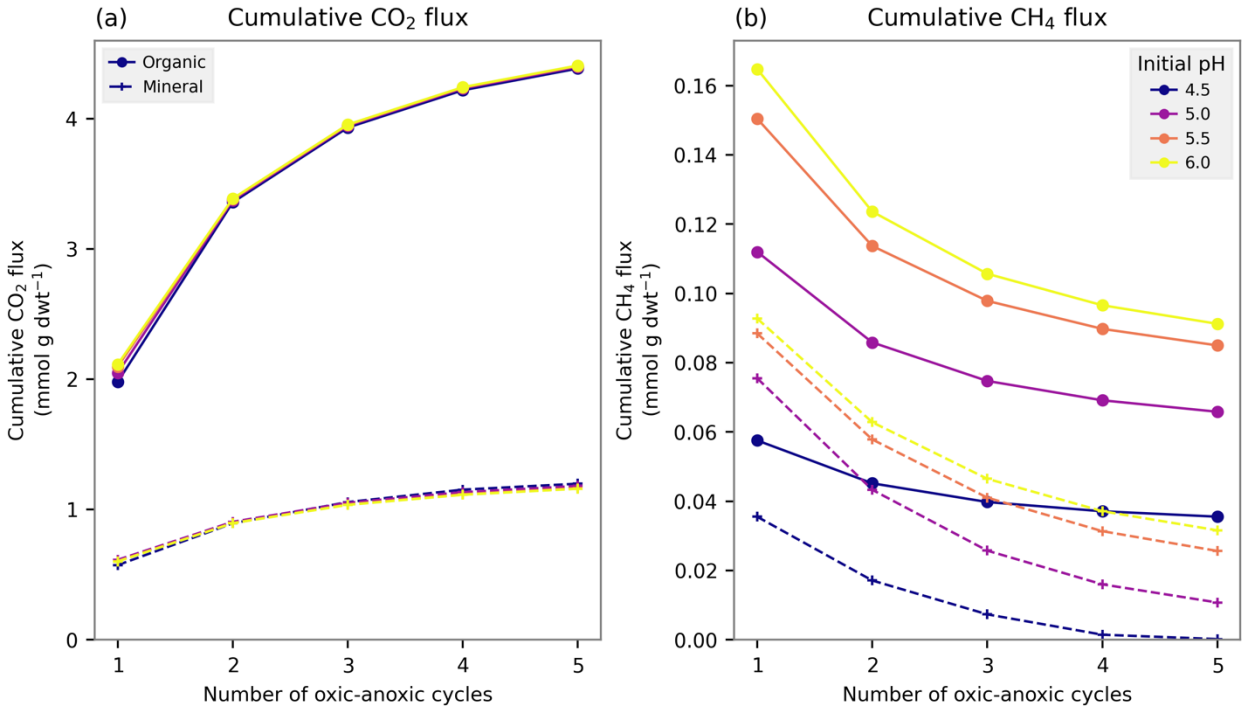

317
318 Figure 4: Integrated CO_2 and CH_4 fluxes over a 150-day period with varying pH and number of
319 oxic-anoxic cycles. Each simulation had a total of 15 days of oxic conditions, divided evenly
320 across the oxic-anoxic cycles. pH is indicated by symbol colors. Solid lines and circles show a
321 simulated organic horizon; dashed lines and pluses show a simulated mineral horizon. (a): CO_2
322 flux. (b): CH_4 flux.

4. Discussion

4.1. Implications for model projections of Arctic carbon cycling

Current Earth system models omit redox interactions such as Fe-C coupling in simulations of SOM degradation, CO_2 emissions, and CH_4 production (Wania et al., 2013). Most models simulate CH_4 production as a function of soil respiration, water content, and temperature. Our results suggest that models omitting redox processes such as Fe-C interactions could substantially overestimate CH_4 production and underestimate both CO_2 production and SOM decomposition in soils subject to water table fluctuations, particularly under acidic pH conditions. Our simulations confirm previous findings that Fe cycling under oxic and anoxic conditions driven by water table variation is an important driver of permafrost C cycling (Lipson et al., 2012). One model, CLM4Me (Riley et al., 2011), does include a parameterization of depletion of alternative terminal electron acceptors, which is simulated as a delayed increase in CH_4 production rate with a characteristic time scale of 30 days. While incorporating a temporal delay between the onset of anoxic conditions and maximum CH_4 production can partially mitigate overestimates of CH_4 production, such models depend on simplified parameterizations of the delay length and cannot easily accommodate the effects of variations in pH and Fe availability in different soils. Our results suggest that both the length and the strength of CH_4 emission suppression depend strongly on pH and the availability and solubility of Fe(III) oxide minerals (Fig. 3). Our results are consistent with previous model simulations of permafrost biogeochemical dynamics, which have highlighted the importance of pH buffering capacity (Tang, Zheng, et al., 2016; Zheng et al., 2019). Our simulations extend previous model applications by simulating fluctuations in oxygen availability which serve as proxies for hydrological transitions. Furthermore, our simulations use a model with an existing interface to a full-featured land surface model (Tang, Yuan, et al., 2016), providing a pathway toward integrating detailed biogeochemical dynamics into large-scale model simulations.

Thawing permafrost undergoes substantial changes in hydrology that can drive varying biogeochemical processes, including flooding of collapsed permafrost (Turetsky et al., 2020) and drying of deeper thawed soil layers under warming (Pegoraro et al., 2020). While projections of how hydrology of permafrost itself will change are a grand challenge for predicting the future of Arctic systems (Walvoord & Kurylyk, 2016), the impacts of hydrological changes on

biogeochemical cycles represent their own set of challenges for predictive modeling. Hydrological changes driven by permafrost thaw can drive rapid organic matter losses (O'Donnell et al., 2012) and increases in CO_2 and CH_4 emissions (Natali et al., 2015). The complex and rapidly-changing hydrological patterns in thawing permafrost systems can drive dynamic water tables that make predictions of biogeochemical cycling particularly challenging, but emerging hydrological model frameworks are allowing more accurate simulations of permafrost hydrology (Jan et al., 2018; Painter et al., 2013). Our biogeochemical model framework builds the groundwork for coupling next-generation hydrological simulations to biogeochemical dynamics for improved simulation of biogeochemical cycling in thawing permafrost.

4.2. Factors not considered

Our simulations did not explicitly include the role of organic matter sorption onto reactive Fe oxide surfaces as a stabilization process for soil carbon. Both stabilization of OM through sorption and destabilization of sorbed OM by dissolution of iron oxides under anoxic conditions have been recently highlighted as important components of permafrost soil C cycling (Opfergelt, 2020; Patzner et al., 2020). While the focus of the present study was on short-term CH_4 and CO_2 production rather than SOC stabilization processes, the explicit representation of Fe oxide mineral precipitation and dissolution processes and their dependence on pH and redox conditions makes this model framework well suited to incorporating SOC stabilization effects of Fe oxides in the future. The assumption that Fe(III) reduction occurs in the aqueous phase may also ignore the role of direct microbial interactions with Fe oxide mineral surfaces and formation of biofilms (Roden and Zachara, 1996). Including additional Fe oxide phases beyond $Fe(OH)_3$ could also allow more exploration of how variations in mineral properties such as specific surface area and solubility affect coupled Fe-C cycling. Soil humic acids, such as quinones, are not considered as terminal electron acceptors here. Similarly, the present model does not include nutrient cycling, but would be well suited to represent N cycle processes such as nitrification and denitrification as well as the role of Fe oxides in sequestering phosphorus in Arctic soils (Herndon et al., 2019; Herndon et al., 2020). This model also does not account for microbial biomass production and maintenance, which assimilates a portion of reduced substrate and nutrients, releasing oxidized products.

Our model framework assumed that available Fe(III) directly inhibited methanogenesis. This approach is consistent with the redox ladder conceptual model, and with studies finding suppression of methanogenesis following Fe(III) additions (Reiche et al., 2008; Miller et al., 2015), but may not adequately reproduce previous observations of positive correlations between Fe(III) reduction and methanogenesis (Herndon et al., 2015; Yang et al., 2016). Simultaneous Fe(III) reduction and methanogenesis could be accommodated by the present model framework by increasing the relative value of inhibition constants (K_I) for methanogenesis relative to half-saturation constants (K_S) for Fe(III) reduction. An alternative approach would be directly simulating competition for electron donor substrates (Lovely, 1991) instead of direct inhibition of reaction rates.

Our simulations focused on a single soil layer and did not include vertical variations in soil properties or vertical transport of gases such as O_2, CO_2, or CH_4. Thus, they omitted potentially important effects such as water table fluctuations and methanotrophy. Aerobic methanotrophy reduces net methane fluxes in oxic and suboxic layers, while anaerobic methane oxidiation can slowly remove methane in anoxic layers. The oxic-anoxic cycles in the current model could be viewed as a time-for-space substitution approach for characterizing soil transition zones close to a dynamic water table. A vertically resolved model would allow more realistic simulations of how the key Fe-C interactions we identified act across vertical oxic-anoxic transitions in soils. More explicit vertically resolved simulations are planned as a next step with this model framework. Future applications of the model that include transport and vertical interactions, will make direct comparisons with field measurements more straightforward.

5. Conclusions

We developed a biogeochemical model framework to represent interactions among carbon, Fe minerals, and pH dynamics in iron-rich Arctic soils. The model reproduced CO_2 and CH_4 emission patterns along with pH and Fe redox dynamics from oxic and anoxic laboratory incubations. Simulations of repeated oxic-anoxic cycles showed that Fe(III) reduction could suppress CH_4 and enhance CO_2 production when oxic-anoxic cycles were more frequent, because reducible Fe was renewed during oxic periods and served as a preferential electron acceptor at the beginning of each anoxic period. The effects of Fe on CO_2 and CH_4 emissions

were stronger under lower pH conditions. Our results suggest that models that omit Fe and other terminal electron acceptors could overestimate CH_4 production and underestimate CO_2 production in systems with dynamic water tables, and that site-specific chemical factors including pH, bulk density, and Fe availability may be necessary for accurate simulations of C cycle dynamics and greenhouse gas emissions from hydrologically dynamic Arctic soils.

Acknowledgements:

The NGEE Arctic project is supported by the Office of Biological and Environmental Research in the US Department of Energy's Office of Science. This research used resources of the Compute and Data Environment for Science (CADES) at the Oak Ridge National Laboratory, which is supported by the Office of Science of the U.S. Department of Energy under Contract No. DE-AC05-00OR22725. JZ is supported by COMPASS-FME, a multi-institutional project supported by the U.S. Department of Energy, Office of Science, Biological and Environmental Research as part of the Environmental System Science Program. The Pacific Northwest National Laboratory is operated for DOE by Battelle Memorial Institute under contract DE-AC05-76RL01830. Thanks to Erin Berns for helpful comments on the manuscript.

Data availability:

Model code, output data, and analysis scripts are archived in the NGEE Arctic Data Repository [doi:10.5440/1814844; Sulman et al., 2021].

6. References

Bockheim, J. G., Hinkel, K. M., & Nelson, F. E. (2003). Predicting carbon storage in tundra soils of Arctic Alaska. *Soil Science Society of America Journal*, *67*(3), 948–950.

Dettling, M. D., Yavitt, J. B., & Zinder, S. H. (2006). Control of organic carbon mineralization by alternative electron acceptors in four peatlands, central New York state, USA. *Wetlands*, *26*(4), 917–927. https://doi.org/10.1672/0277-5212(2006)26[917:COOCMB]2.0.CO;2

Dwivedi, D., Arora, B., Steefel, C. I., Dafflon, B., & Versteeg, R. (2018). Hot Spots and Hot Moments of Nitrogen in a Riparian Corridor. *Water Resources Research*, *54*(1), 205–222.

https://doi.org/10.1002/2017WR022346
Hammond, G. E., Lichtner, P. C., & Mills, R. T. (2014). Evaluating the performance of parallel subsurface simulators: An illustrative example with PFLOTRAN. *Water Resources Research*, *50*(1), 208–228. https://doi.org/10.1002/2012WR013483
Herndon, E. M., Yang, Z., Bargar, J., Janot, N., Regier, T. Z., Graham, D. E., et al. (2015). Geochemical drivers of organic matter decomposition in Arctic tundra soils. *Biogeochemistry*, *126*(3), 397–414. https://doi.org/10.1007/s10533-015-0165-5
Herndon, E. M., Yang, Z., Graham, D. E., Wullschleger, S. D., Gu, B., & Liang, L. (2016). Surface and Active Layer Pore Water Chemistry from Ice Wedge Polygons, Barrow, Alaska, 2013-2014. Oak Ridge, TN: Next Generation Ecosystem Experiments Arctic Data Collection, Oak Ridge National Laboratory. https://doi.org/10.5440/1226245
Herndon, E. M., AlBashaireh, A., Singer, D., Roy Chowdhury, T., Gu, B., & Graham, D. (2017). Influence of iron redox cycling on organo-mineral associations in Arctic tundra soil. *Geochimica et Cosmochimica Acta*, *207*, 210–231. https://doi.org/10.1016/j.gca.2017.02.034
Herndon, E. M., Kinsman-Costello, L., Duroe, K. A., Mills, J., Kane, E. S., Sebestyen, S. D., et al. (2019). Iron (oxyhydr)oxides serve as phosphate traps in tundra and boreal peat soils. *Journal of Geophysical Research: Biogeosciences*. https://doi.org/10.1029/2018JG004776
Herndon, E., Kinsman-Costello, L., Di Domenico, N., Duroe, K., Barczok, M., Smith, C., & Wullschleger, S. D. (2020). Iron and iron-bound phosphate accumulate in surface soils of ice-wedge polygons in arctic tundra. *Environmental Science. Processes & Impacts*, *22*(7), 1475–1490. https://doi.org/10.1039/d0em00142b
Hugelius, G., Strauss, J., Zubrzycki, S., Harden, J. W., Schuur, E. A. G., Ping, C. L., et al. (2014). Estimated stocks of circumpolar permafrost carbon with quantified uncertainty ranges and identified data gaps. *Biogeosciences*, *11*(23), 6573–6593. https://doi.org/10.5194/bg-11-6573-2014
Jan, A., Coon, E. T., Painter, S. L., Garimella, R., & Moulton, J. D. (2018). An intermediate-scale model for thermal hydrology in low-relief permafrost-affected landscapes. *Computational Geosciences*, *22*(1), 163–177. https://doi.org/10.1007/s10596-017-9679-3
Kotsyurbenko, O. R., M. W. Friedrich, M. V. Simankova, A. N. Nozhevnikova, P. N. Golyshin, K. N. Timmis, and R. Conrad (2007). Shift from Acetoclastic to H_2-Dependent

475 Methanogenesis in a West Siberian Peat Bog at Low pH Values and Isolation of an
476 Acidophilic Methanobacterium Strain. *Applied and Environmental Microbiology* 73 (7):
477 2344–48. https://doi.org/10.1128/AEM.02413-06.
478 Lipson, D. A., Jha, M., Raab, T. K., & Oechel, W. C. (2010). Reduction of iron (III) and humic
479 substances plays a major role in anaerobic respiration in an Arctic peat soil. *Journal of*
480 *Geophysical Research: Biogeosciences*, *115*(4), 1–13.
481 https://doi.org/10.1029/2009JG001147
482 Lipson, D. A., Zona, D., Raab, T. K., Bozzolo, F., Mauritz, M., & Oechel, W. C. (2012). Water-
483 table height and microtopography control biogeochemical cycling in an Arctic coastal
484 tundra ecosystem. *Biogeosciences*, *9*(1), 577–591.
485 Lovley, D. R. (1991). Dissimilatory Fe(III) and Mn(IV) reduction. *Microbiological Reviews*,
486 *55*(2), 259–287. https://doi.org/10.1128/mr.55.2.259-287.1991
487 Miller, K. E., Lai, C.-T., Friedman, E. S., Angenent, L. T., & Lipson, D. A. (2015). Methane
488 suppression by iron and humic acids in soils of the Arctic Coastal Plain. *Soil Biology &*
489 *Biochemistry*, *83*, 176–183. https://doi.org/10.1016/j.soilbio.2015.01.022
490 Natali, S. M., Schuur, E. A. G., Mauritz, M., Schade, J. D., Celis, G., Crummer, K. G., et al.
491 (2015). Permafrost thaw and soil moisture driving CO_2 and CH_4 release from upland tundra.
492 *Journal of Geophysical Research: Biogeosciences*, *120*(3), 525–537.
493 https://doi.org/10.1002/2014JG002872
494 O'Donnell, Jonathan A., M. Torre Jorgenson, Jennifer W. Harden, A. David McGuire, Mikhail
495 Z. Kanevskiy, and Kimberly P. Wickland. 2012. The Effects of Permafrost Thaw on Soil
496 Hydrologic, Thermal, and Carbon Dynamics in an Alaskan Peatland. *Ecosystems* 15 (2):
497 213–29. https://doi.org/10.1007/s10021-011-9504-0.
498 Opfergelt, S. (2020). The next generation of climate model should account for the evolution of
499 mineral-organic interactions with permafrost thaw. *Environmental Research Letters*, *15*(9).
500 https://doi.org/10.1088/1748-9326/ab9a6d
501 Painter, S. L., Moulton, J. D., & Wilson, C. J. (2013). Modeling challenges for predicting
502 hydrologic response to degrading permafrost. *Hydrogeology Journal*, *21*(1), 221–224.
503 https://doi.org/10.1007/s10040-012-0917-4

Patzner, M. S., Mueller, C. W., Malusova, M., Baur, M., Nikeleit, V., Scholten, T., et al. (2020). Iron mineral dissolution releases iron and associated organic carbon during permafrost thaw. *Nature Communications*, *11*(1), 6329. https://doi.org/10.1038/s41467-020-20102-6

Pegoraro, E. F., Mauritz, M. E., Ogle, K., Ebert, C. H., & Schuur, E. A. G. (2020). Lower soil moisture and deep soil temperatures in thermokarst features increase old soil carbon loss after 10 years of experimental permafrost warming. *Global Change Biology*, gcb.15481. https://doi.org/10.1111/gcb.15481

Ping, C. L., Bockheim, J. G., Kimble, J. M., Michaelson, G. J., & Walker, D. A. (1998). Characteristics of cryogenic soils along a latitudinal transect in arctic Alaska. *Journal of Geophysical Research*, *103*(D22), 28917–28928. https://doi.org/10.1029/98jd02024

Reiche, M., Torburg, G., & Küsel, K. (2008). Competition of Fe(III) reduction and methanogenesis in an acidic fen. *FEMS Microbiology Ecology*, *65*(1), 88–101. https://doi.org/10.1111/j.1574-6941.2008.00523.x

Riley, W. J., Subin, Z. M., Lawrence, D. M., Swenson, S. C., Torn, M. S., Meng, L., et al. (2011). Barriers to predicting changes in global terrestrial methane fluxes: analyses using CLM4Me, a methane biogeochemistry model integrated in CESM. *Biogeosciences*, *8*(7), 1925–1953. https://doi.org/10.5194/bg-8-1925-2011

Roden, E. E., & Zachara, J. M. (1996). Microbial Reduction of Crystalline Iron(III) Oxides: Influence of Oxide Surface Area and Potential for Cell Growth. *Environmental Science & Technology*, *30*(5), 1618–1628. https://doi.org/10.1021/es9506216

Roy Chowdhury, T., Herndon, E. M., Phelps, T. J., Elias, D. A., Gu, B., Liang, L., et al. (2015). Stoichiometry and temperature sensitivity of methanogenesis and CO2 production from saturated polygonal tundra in Barrow, Alaska. *Global Change Biology*, *21*(2), 722–737. https://doi.org/10.1111/gcb.12762

Schädel, C., Luo, Y., David Evans, R., Fei, S., & Schaeffer, S. M. (2013). Separating soil CO2 efflux into C-pool-specific decay rates via inverse analysis of soil incubation data. *Oecologia*, *171*(3), 721–732. https://doi.org/10.1007/s00442-012-2577-4

Schuur, E. A. G., McGuire, A. D., Schädel, C., Grosse, G., Harden, J. W., Hayes, D. J., et al. (2015). Climate change and the permafrost carbon feedback. *Nature*, *520*(7546), 171–179. https://doi.org/10.1038/nature14338

Sulman, B. N., Yuan, F., O'Meara, T., Graham, D., Gu, B., Herndon, H., Zheng, J. 2021. Iron

cycle interactions with hydrological dynamics reduce methane production in a simulated Arctic soil: Modeling Archive. Next Generation Ecosystem Experiments Arctic Data Collection, Oak Ridge National Laboratory, U.S. Department of Energy, Oak Ridge, Tennessee, USA. https://doi.org/10.5440/1814844.

Tang, G., Yuan, F., Bisht, G., Hammond, G. E., Lichtner, P. C., Kumar, J., et al. (2016). Addressing numerical challenges in introducing a reactive transport code into a land surface model: A biogeochemical modeling proof-of-concept with CLM-PFLOTRAN 1.0. *Geoscientific Model Development*, *9*(3), 927–946. https://doi.org/10.5194/gmd-9-927-2016

Tang, G., Zheng, J., Xu, X., Yang, Z., Graham, D. E., Gu, B., et al. (2016). Biogeochemical modeling of CO2 and CH4 production in anoxic Arctic soil microcosms. *Biogeosciences*, *13*(17), 5021–5041. https://doi.org/10.5194/bg-13-5021-2016.

Throckmorton, H. M., Heikoop, J. M., Newman, B. D., Altmann, G. L., Conrad, M. S., Muss, J. D., et al. (2015). Pathways and transformations of dissolved methane and dissolved inorganic carbon in Arctic tundra watersheds: Evidence from analysis of stable isotopes. *Global Biogeochemical Cycles*, *29*(11), 1893–1910. https://doi.org/10.1002/2014GB005044

Turetsky, M. R., Abbott, B. W., Jones, M. C., Anthony, K. W., Olefeldt, D., Schuur, E. A. G., et al. (2020). Carbon release through abrupt permafrost thaw. *Nature Geoscience*, *13*(2), 138–143. https://doi.org/10.1038/s41561-019-0526-0

Walvoord, M. A., & Kurylyk, B. L. (2016). Hydrologic Impacts of Thawing Permafrost-A Review. *Vadose Zone Journal*, *15*(6), vzj2016.01.0010. https://doi.org/10.2136/vzj2016.01.0010

Wang, Y., Yuan, F., Yuan, F., Gu, B., Hahn, M. S., Torn, M. S., et al. (2019). Mechanistic Modeling of Microtopographic Impacts on CO2 and CH4 Fluxes in an Alaskan Tundra Ecosystem Using the CLM-Microbe Model. *Journal of Advances in Modeling Earth Systems*, *11*(12), 4288–4304. https://doi.org/10.1029/2019MS001771

Wania, R., Melton, J. R., Hodson, E. L., Poulter, B., Ringeval, B., Spahni, R., et al. (2013). Present state of global wetland extent and wetland methane modelling: Methodology of a model inter-comparison project (WETCHIMP). *Geoscientific Model Development*, *6*(3), 617–641. https://doi.org/10.5194/gmd-6-617-2013

Xu, X., Yuan, F., Hanson, P. J., Wullschleger, S. D., Thornton, P. E., Riley, W. J., et al. (2016). Reviews and syntheses: Four decades of modeling methane cycling in terrestrial

ecosystems. *Biogeosciences*, *13*(12), 3735–3755. https://doi.org/10.5194/bg-13-3735-2016

Yang, Z., Wullschleger, S. D., Liang, L., Graham, D. E., & Gu, B. (2016). Effects of warming on the degradation and production of low-molecular-weight labile organic carbon in an Arctic tundra soil. *Soil Biology & Biochemistry*, *95*, 202–211. https://doi.org/10.1016/j.soilbio.2015.12.022

Zheng, J., RoyChowdhury, T., Herndon, E. M., Yang, Z., Gu, B., Wullschleger, S., & Graham, D. (2018). Synthesis of Soil Geochemical Characteristics and Organic Carbon Degradation from Arctic Polygon Tundra, Barrow, Alaska. Oak Ridge, TN: Next Generation Ecosystem Experiments Arctic Data Collection, Oak Ridge National Laboratory. https://doi.org/10.5440/1440029

Zheng, J., RoyChowdhury, T., Yang, Z., Gu, B., Wullschleger, S. D., & Graham, D. E. (2018). Impacts of temperature and soil characteristics on methane production and oxidation in Arctic tundra. *Biogeosciences* , *15*(21), 6621–6635. https://doi.org/10.5194/bg-15-6621-2018

Zheng, J., Thornton, P. E., Painter, S. L., Gu, B., Wullschleger, S. D., & Graham, D. E. (2019). Modeling anaerobic soil organic carbon decomposition in Arctic polygon tundra: insights into soil geochemical influences on carbon mineralization. *Biogeosciences*, *16*(3), 663–680. https://doi.org/10.5194/bg-16-663-2019